

2 **Collide and Conquer: Constraints on Simplified Dark** 3 **Matter Models using Mono- X Collider Searches**

4 **A. J. Brennan,^{a,1} M. F. McDonald,^a J. Gramling^b and T. D. Jacques^c**

5 ^a*The University of Melbourne, Parkville 3010, Australia*

6 ^b*Université de Genève, Quai E. Ansermet 24, 1211 Genève 4, Switzerland*

7 ^c*SISSA/ISAS, via Bonomea 265, 34136 Trieste, Italy*

8 *E-mail:* amelia.brennan@coepp.org.au, millie.mcdonald@coepp.org.au,
johanna.gramling@cern.ch, thomas.jacques@sissa.it

9 ABSTRACT: The use of simplified models of dark matter is becoming increasingly prevalent
10 in collider searches, and while early Run II results are beginning to appear, we look to see
11 what further information can be extracted from Run I results. We consider three ‘standard’
12 simplified models that couple quarks to fermionic singlet dark matter: an s -channel vector
13 mediator with vector or axial-vector couplings, and a t -channel scalar mediator. Upper lim-
14 its on the couplings are calculated, and compared across three alternate channels, namely,
15 mono-jet, mono- Z (leptonic) and mono- W/Z (hadronic). The strongest limits are observed
16 in the mono-jet channel, however the computational simplicity, and absence of significant
17 t -channel model width effects, in the mono-boson channels make these a straightforward
18 and fast alternative.

¹Corresponding author.

| | | |
|----|-------------------------------------------------------------------------|-----------|
| 19 | Contents | |
| 20 | 1 Introduction | 2 |
| 21 | 2 Simplified Model Phenomenology | 3 |
| 22 | 2.1 Model Descriptions | 3 |
| 23 | 2.2 The Mono- $X + E_{\text{T}}^{\text{miss}}$ Signature | 4 |
| 24 | 2.3 Mass and Coupling Points | 5 |
| 25 | 2.4 Treatment of the width | 6 |
| 26 | 3 Recasting mono-X constraints | 8 |
| 27 | 3.1 Signal Simulation | 9 |
| 28 | 3.1.1 Parton Matching Scheme | 9 |
| 29 | 3.2 Mono-jet Constraints | 9 |
| 30 | 3.3 Mono- Z Constraints | 10 |
| 31 | 3.4 Mono- W/Z Constraints | 11 |
| 32 | 4 Results and Discussion | 12 |
| 33 | 4.1 Limits on the coupling $\sqrt{g_q g_\chi}$ | 12 |
| 34 | 4.1.1 Mono-jet channel | 13 |
| 35 | 4.1.2 Mono- Z channel | 14 |
| 36 | 4.1.3 Mono- W/Z channel | 14 |
| 37 | 4.2 Comparison with Relic Density Constraints | 15 |
| 38 | 4.3 Comparison with Direct Detection Constraints | 15 |
| 39 | 4.4 Discussion | 21 |
| 40 | 5 Conclusion | 21 |
| 41 | 6 Acknowledgements | 21 |
| 42 | A Limit setting strategy | 21 |
| 43 | A.1 Nominal Values | 21 |
| 44 | A.2 Uncertainty Estimation | 22 |
| 45 | B Validation of signal simulation and event selection procedures | 23 |
| 46 | B.1 Monojet Channel | 23 |
| 47 | B.2 Mono- Z Channel | 23 |
| 48 | B.3 Mono- W/Z Channel | 24 |

1 Introduction

Simplified models have emerged as a powerful tool for the interpretation of collider, direct and indirect detection signals of dark matter (DM). Previously, ATLAS and CMS searches for DM were conducted within the context of both Effective Field Theories (EFTs) [1, 5, 32, 33] and full UV-complete theories such as Supersymmetry [10–12, 40]. I suggest we just list official ATLAS and CMS studies here to avoid ‘opening the floodgates’, so I’ve removed a few references - TJ. The latter approach, though well-motivated, is typified by a broad parameter space and generally yields results which are insensitive to the wider class of DM models. EFT constraints, in comparison, are applicable to a broad range of models and rely on the specification of only a small set of parameters, namely the suppression scale, M_\star , and the DM mass, m_{DM} [25]. In the EFT framework, interactions between the dark and Standard Model (SM) sector are parametrised by a set of higher-dimensional effective operators, that arise when the mass of the mediating particle is assumed to be significantly larger than the momentum transferred in a given interaction. Where this is not the case, the EFT prescription can produce constraints which detour dramatically from those of the associated UV-complete model [24–28]. This is not so important in direct detection experiments where the momentum transferred in the scattering of DM particles with heavy nuclei is generally of the order of tens of MeV [13, 14], or in indirect searches where the annihilations of non-relativistic DM particles in the galactic halo occur with momentum transfers of order m_{DM} []. However, for hadron collider searches - where the accessible center of mass energy of two colliding baryons may be sufficient to produce the mediator on-shell - the range of validity of the EFT prescription is significantly diminished. Indeed, recent works have shown the EFT approach to be problematic in certain cases for the interpretation of data collected during the $\sqrt{s} = 8$ TeV Run I of the Large Hadron Collider (LHC) [15–17]. In light of this, simplified models have become the preferred tool for the interpretation of collider DM searches [18, 31, 53, 55, 56].

In a nutshell, a simplified model (SiM) arises when the heavy mediator which was integrated out in the EFT framework is reintroduced. Like EFTs, SiMs admit the comparison of results obtained in the different avenues of dark matter study [] and are defined by a relatively small set of parameters - namely m_{DM} , the mass of the mediator M_{med} , and the SM-mediator and DM-mediator coupling strengths, g_q and g_χ (or $g_{q\chi}$ in the case of a single, SM-DM-mediator coupling). Unlike EFTs, constraints calculated within the context of a SiM are valid across a broad energy range.

In this paper, we examine a phenomenologically distinct set of SiMs. In particular, we place constraints on the SiMs corresponding to the simplest UV-completions of the D5 (vector) and D8 (axial-vector) effective operators in the s -channel¹. We also include a case

¹The D5 and D8 operators form a nice starting point in the analysis of simplified models as they have been studied exhaustively in the past (see refs. [1, 4, 5, 7, 15–17, 32, 33] among others). This attention is motivated by the fact that collider limits for the D5 (D8) operator can be readily transformed into limits on spin-independent (spin-dependent) DM-nucleon scattering and vice versa. With the exception of D1 (see sec. ??), and D9 and D11 (which have no simple simplified model counterparts []), the remaining effective operators induce elastic scattering which is suppressed by powers of the DM velocity or the momentum transferred [19]. Hence, these operators are not often considered in the literature.

in which a scalar mediator is exchanged in the t -channel, motivated by its analog of squark exchange in Supersymmetry. In the heavy mediator limit, this model can be expressed as a combination of operators D5 to D8 via a Fierz transformation.

The models are constrained using public results from mono- X + missing transverse energy ($E_{\text{T}}^{\text{miss}}$) searches conducted by the ATLAS Collaboration. Specifically we focus on searches where X is either a parton (manifesting in the detector as a narrow-radius jet), a leptonically-decaying Z boson, or a hadronically-decaying W or Z boson (manifesting as a large-radius jet). The purpose of this work is to strengthen existing SiM limits [23, 57] using the full 20.3 fb^{-1} of Run I ATLAS data, and to explore an enhanced phase space with respect to the mediator and DM masses and the relative strength of the couplings to the visible and dark sectors. We choose to treat the mediator width as the minimal value naturally arising, which is more realistic than a fixed width. We extend the study by providing a cross-check and comparison of the performance of the three targeted collider detection channels, and compare against relic density and direct detection constraints.

The remainder of the paper is organised as follows. Section 2 contains a compendium of the SiMs chosen for analysis and the associated collider phenomenology. Section 3 outlines the techniques used to recast mono- X + $E_{\text{T}}^{\text{miss}}$ limits on the visible cross-section for any new physics process into constraints on SiMs, and specifically on the couplings g_q and g_χ . Lastly, our results are presented in Section 4 along with a discussion of the implications of this work. Appendices A and B include details of the limit setting and analysis validation procedures.

2 Simplified Model Phenomenology

2.1 Model Descriptions

We begin with a short set of assumptions: that the DM particle, χ , is a weakly interacting Dirac fermion, that it is a singlet under the SM, and that it is the lightest stable new particle. Additionally the new sector is assumed to couple only to the SM quarks; while possible coupling to SM leptons e.g. [26] or gluons e.g. [59] has been studied elsewhere, it is beyond the scope of this paper. The nature of the mediating particle then results from these assumptions: in the s -channel it is chosen to be a vector particle and must also be a SM singlet, denoted ξ , while in the t -channel it is identified as scalar and is necessarily charged and coloured, and labelled ϕ .

The s -channel models chosen for analysis are characterised by vector (sV) or axial-vector (sA) couplings to both the dark and SM sectors. They are described by the following interaction Lagrangians:

$$\mathcal{L}_{sV} \supset -\xi_\mu \left[\sum_q g_q \bar{q} \gamma^\mu q - g_\chi \bar{\chi} \gamma^\mu \chi \right], \quad (2.1)$$

$$\mathcal{L}_{sA} \supset \xi_\mu \left[\sum_q g_q \bar{q} \gamma^\mu \gamma_5 q - g_\chi \bar{\chi} \gamma^\mu \gamma_5 \chi \right], \quad (2.2)$$

where the sum is over all quarks. For the couplings g_q and g_χ to remain within the perturbative regime, they are required to satisfy $g_q, g_\chi \leq 4\pi$, though stronger perturbativity requirements do exist [15].

The t -channel model considered in this paper (abbreviated tS) is characterised by a scalar mediator and is motivated by analogy with a common aspect of Supersymmetric models: neutralino DM interacting with the SM sector via t -channel exchange of a squark [20]. Note that in this Supersymmetric scenario the DM particle is a Majorana fermion. The collider phenomenology of SiMs in which χ is of Majorana type is kinematically identical to the corresponding Dirac cases (requiring multiplication of the cross-section by a simple factor in order to compute limits) and so are not covered here². The exception to this rule is the s -channel vector mediator model, which vanishes if χ is a Majorana fermion [21].

In the tS model, the mediator is allowed to couple to either the left or right-handed quarks as an $SU(2)$ doublet or singlet respectively. Since the LHC is insensitive to the chirality of the quarks, we assume for simplicity that ϕ couples to the left-handed quarks only, and is itself an $SU(2)$ doublet, allowing radiation of a W boson. To avoid different couplings to quarks of different generations, and to remain in step with the DM forum recommendations [53], we include three generations of mediator ϕ , with equal masses and couplings. The interaction Lagrangian for this model is then:

$$\mathcal{L}_{tS} \supset \sum_Q g_{q\chi} \bar{Q} P_R \phi \chi + \text{h.c.}, \quad (2.3)$$

where the sum is over the three quark doublets, $g_{q\chi}$ is the scalar coupling of the incoming quark, ϕ and χ , and P_R is the usual chiral projection operator. **Should ϕ have a subscript Q here?**

2.2 The Mono- $X + E_T^{\text{miss}}$ Signature

The mono- $X + E_T^{\text{miss}}$ (abbreviated to mono- X) is a popular collider signal in the search for new physics, particularly in the search for dark matter. Since DM particles are not expected to interact with detector material, they appear as missing transverse energy when balanced against a visible object, X , that is radiated from the initial or intermediate state (where the latter is permitted in the t -channel model). For the s -channel SiMs discussed above, only initial-state radiation is permitted; see figs. 1a and 1b for examples. For the tS model, radiation of a gluon or electroweak (EW) boson is permitted both from initial state partons (fig. 1c) or from the mediator (fig. 1d).

The most likely scenario at the LHC is production of a jet alongside the invisible χ pair, as a result of the strong coupling and prevalence of partons in the initial state. However, to fully exploit the potential of the ATLAS detector to record and identify a vast array of particle types, we can include the alternative mono- W/Z channels to potentially glean further information. We can take advantage of the relative cleanliness and simplicity of leptons in the leptonically-decaying mono- Z channel, or the large hadronic

²The exception being in the validation of the mono- Z channel, see Sec. B.2.

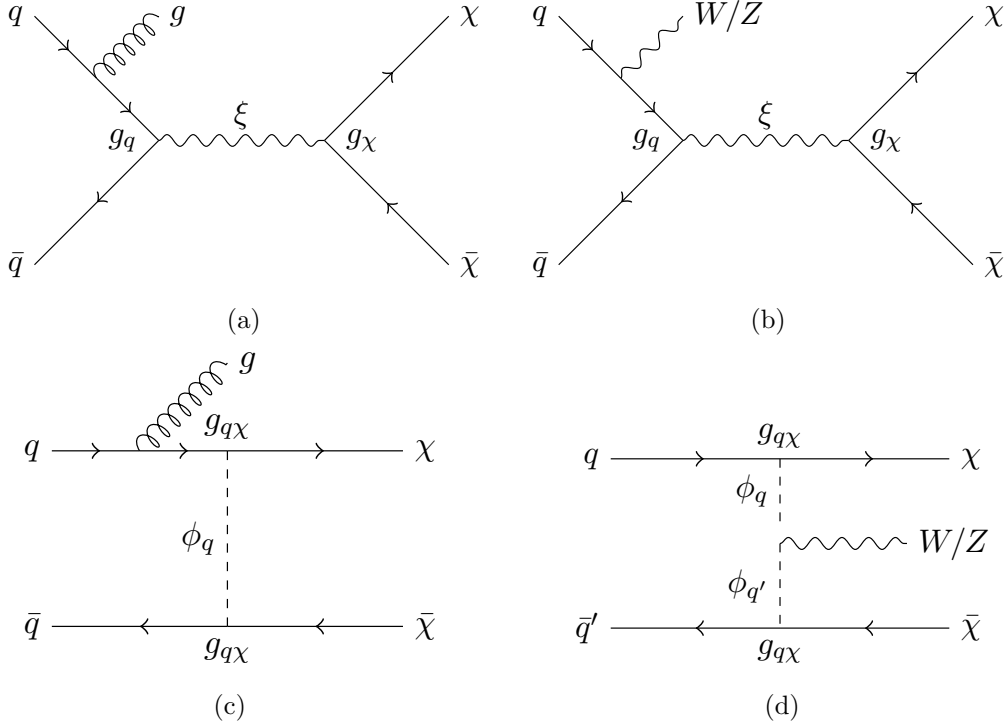


Figure 1: Representative dark matter pair-production processes with a gluon or W/Z boson in the final state for the s -channel (a,b) and t -channel (c,d) models.

157 branching fraction, and developing techniques to identify jets resulting from EW bosons,
 158 in the hadronically-decaying mono- W/Z channel³. In both cases, the large multi-jet back-
 159 ground is reduced, and complications in jet production such as parton-matching can be
 160 ignored, making these an interesting alternative where speed, efficiency and a reduction in
 161 jet-associated uncertainties may make up for the loss in sensitivity.

162 2.3 Mass and Coupling Points

163 A representative set of dark matter and mediator masses, listed in table 1, are chosen for
 164 study in each detection channel. DM masses of 3, 30 and 300 GeV were also included in the
 165 mono- Z channel, where ease of production can afford higher granularity. All (m_χ, M_{med})
 166 combinations are permitted in the sV and sA models, while in the tS model M_{med} must
 167 be greater than m_χ to ensure stability of the DM particle. The couplings g_q and $g_{q\chi}$ are
 168 set to unity, while the DM-mediator coupling in the s -channel models, g_χ , was varied from
 169 0.2 to 5. The mediator masses are chosen to cover a broad range of parameter space and
 170 to coincide with predominantly three regimes: (near-)degenerate ($M_{\text{med}} \approx m_\chi$), on-shell
 171 ($M_{\text{med}} \geq 2m_\chi$) and off-shell ($M_{\text{med}} < 2m_\chi$).

³In addition, one of the first Run II dark matter search results from ATLAS was from this channel [60], released during the preparation of this paper.

| m_χ [GeV] | M_{med} [GeV] | s-channel | | t-channel |
|---------------------------------------|---------------------------------------|-----------|----------------------|-------------|
| | | g_q | g_χ | $g_{q\chi}$ |
| 1, (3), 10, (30), 100, (300), 1000 | 1, 2, 10, 20, 100, 200, 1000, 2000 | 1 | 0.2, 0.5, 1, 2, 5 | 1 |

Table 1: Mass and coupling points chosen for the analysis of simplified dark matter models. Values in brackets are only included in the mono- Z channel. The mediator masses are primarily representative of three regimes: (near-)degenerate ($M_{\text{med}} \approx m_\chi$), on-shell ($M_{\text{med}} \geq 2m_\chi$) and off-shell ($M_{\text{med}} < 2m_\chi$). For the t -channel model, $M_{\text{med}} > m_\chi$ is required to ensure stability of the DM particle.

2.4 Treatment of the width

An important factor when considering simplified models is to ensure the mediator width is treated appropriately, as it impacts both the cross-section calculation and, in some cases, the kinematic behaviour of the model.

Following the DM Forum recommendations [53], we use the minimal width, allowing coupling to all kinematically accessible quarks. We assume minimal flavour violation, which implies a universal coupling to all quark flavours. The minimum width for each model is given by:

$$\begin{aligned} \Gamma_{sV} = & \frac{g_\chi^2 M}{12\pi} \left(1 + \frac{2m_\chi^2}{M^2}\right) \left(1 - \frac{4m_\chi^2}{M^2}\right)^{\frac{1}{2}} \Theta(M - 2m_\chi) \\ & + \sum_q \frac{g_q^2 M}{4\pi} \left(1 + \frac{2m_q^2}{M^2}\right) \left(1 - \frac{4m_q^2}{M^2}\right)^{\frac{1}{2}} \Theta(M - 2m_q) \end{aligned} \quad (2.4)$$

$$\begin{aligned} \Gamma_{sA} = & \frac{g_\chi^2 M}{12\pi} \left(1 - \frac{4m_\chi^2}{M^2}\right)^{\frac{3}{2}} \Theta(M - 2m_\chi) \\ & + \sum_q \frac{g_q^2 M}{4\pi} \left(1 - \frac{4m_q^2}{M^2}\right)^{\frac{3}{2}} \Theta(M - 2m_q) \end{aligned} \quad (2.5)$$

$$\begin{aligned} \Gamma_{tS} = & \sum_q \frac{g_{q\chi}^2 M}{16\pi} \left(1 - \frac{m_q^2}{M^2} - \frac{m_\chi^2}{M^2}\right) \\ & \times \sqrt{\left(1 - \frac{m_q^2}{M^2} + \frac{m_\chi^2}{M^2}\right)^2 - 4\frac{m_\chi^2}{M^2}} \Theta(M - m_q - m_\chi) \end{aligned} \quad (2.6)$$

It is possible that the mediator may decay to other SM or BSM particles [31], but this is not expected to have a large effect on the kinematic distribution as long as the width

remains relatively small [53]. The generator treatment of the mediator as a Breit-Wigner propagator, rather than a true kinetic propagator, breaks down for large widths [57]. This ref. also showed that for $\Gamma/M \lesssim 0.5$ the following scaling relations approximately hold:

$$\sigma \propto \begin{cases} g_q^2 g_\chi^2 / \Gamma & \text{if } M_{\text{med}} \geq 2m_{\text{DM}} \\ g_q^2 g_\chi^2 & \text{if } M_{\text{med}} < 2m_{\text{DM}} \end{cases} \quad (2.7)$$

in the sV and sA models, and

$$\sigma \propto g_{q\chi}^4 \quad (2.8)$$

in the tS model. When valid, these approximations allow us to greatly simplify our limit calculations, and for this reason, we restrict our primary results to regions of parameter space where $\Gamma/M < 0.5$.

To simplify the procedure further, we can take advantage of the fact that (with the notable exception of the tS model in the mono-jet channel) for each point in (m_χ, M_{med}) phase space, the mediator width (and therefore the couplings) do not greatly affect each model's kinematic behaviour. This is demonstrated in fig. 2, where for the sV (representing both the sV and sA models) and tS models, we plot a simplified $E_{\text{T}}^{\text{miss}}$ distribution, as a proxy for the full selection in each analysis, for two mass points and a demonstrative set of couplings such that $\Gamma < M_{\text{med}}/2$. The $E_{\text{T}}^{\text{miss}}$ distribution is predominantly independent of the mediator width for the s -channel models in the mono-jet channel, and all models in the mono- Z ⁴ channel. However, there is a clear variation in the kinematic behaviour of the tS model in the mono-jet channel, which can be attributed to additional diagrams (accessible only in this channel) featuring a gluon in the initial state and subsequently allowing the mediator to go on-shell. In this scenario, when the resulting quark and DM particle are both small compared to the mediator mass, they share equally its energy leading to a peak in the $E_{\text{T}}^{\text{miss}}$ distribution at approximately half the mediator mass.

In the cases where the model behaviour is independent of the width, we can greatly simplify the calculations by assuming the impact of the selection cuts in each channel is unchanged for each masspoint; that is, independent of the couplings. In this case, a simple rearrangement of eqns. 2.7 and 2.8 allows us to obtain upper limits on the model couplings (see App. A for further details of this calculation).

A proper study of the tS model within the mono-jet channel, where altering the coupling can lead to changed kinematic behaviour, has been performed elsewhere [23], and requires the production of individual samples for each coupling point. This, combined with the challenges associated with including differing orders of α_s , make the generation process computationally expensive compared to the mono- Z and mono- W/Z channels. We therefore exclude an analysis of the tS model in the mono-jet channel in this work.

⁴In this discussion, the mono- W/Z channel can be assumed to follow the same logic as for the mono- Z channel.

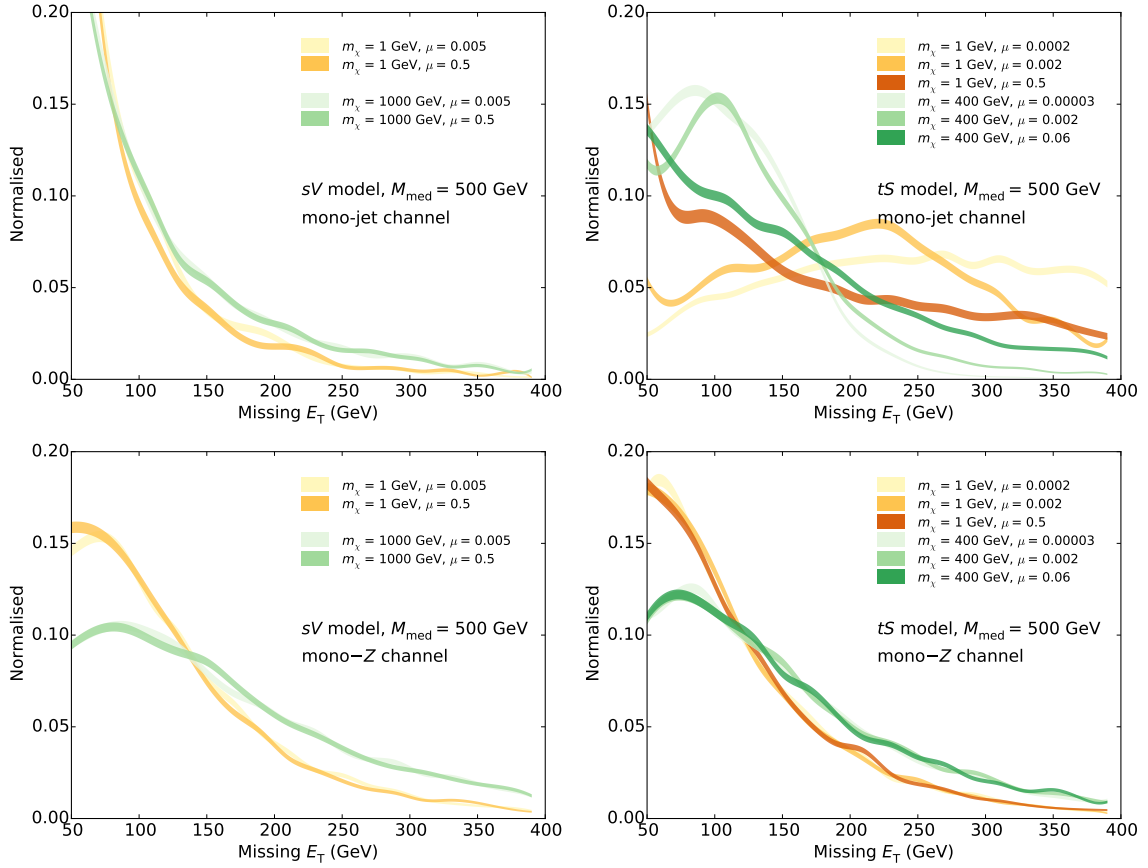


Figure 2: The E_T^{miss} distribution of the sV and tS models in the mono-jet and mono- Z channels, for some demonstrative masses. The parameter μ is defined as Γ/M_{med} , and is used to demonstrate the impact of a changing width; in particular, the tS model in the mono-jet channel shows clear width-dependence. The widths are obtained with couplings of 0.1, 1, and 5 where $\mu < 0.5$ remains true.

214 3 Recasting mono- X constraints

215 The procedure for recasting existing mono- X analyses to obtain SiM constraints follows a
 216 simple cut-and-count methodology. Firstly, signal events are simulated (described below
 217 in section 3.1) with object p_T smearing applied to approximate the detection efficiency of
 218 the ATLAS detector, ϵ . The event selection criteria of the mono- X analysis of interest
 219 is then applied to the simulated signal samples. Events surviving the selection criteria
 220 are counted to determine the likelihood of a dark matter event being observed (referred
 221 to as the acceptance, \mathcal{A}), which is then used in combination with channel-specific model-
 222 independent limits on new physics events to limit the parameter phase space of a given
 223 model. For a comprehensive description of the recasting procedure, see appendix A.

224 In this paper, mono-jet constraints are derived from a search for new phenomena
 225 conducted by the ATLAS Collaboration using pp collisions at $\sqrt{s} = 8$ TeV as described in

ref. [41]. Similarly, the leptonic mono- Z and hadronic mono- W/Z constraints are derived from ATLAS dark matter searches originally optimised for the D1, D5 and D9 effective operators [47, 48]. These analyses are described in further detail in sections 3.2, 3.3 and 3.4 respectively.

3.1 Signal Simulation

Monte Carlo simulated event samples are used to model the expected signal for each channel and for each simplified model. Leading order matrix elements for the process $pp \rightarrow X + \chi\bar{\chi}$ (where X is specifically one or two jets⁵, a $Z(\rightarrow \ell^+\ell^-)$ boson or a $W/Z(\rightarrow jj)$ boson) are first simulated using MADGRAPH5_AMC@NLO v2.2.2 [49] with the MSTW2008lo68cl PDF [50]. During this stage, the renormalisation and factorisation scales are set to the default sum of $\sqrt{m^2 + p_T^2}$ for all particles in the final state. Showering and hadronisation are then performed by PYTHIA 8.201 [58] with the appropriate PDF and using the ATLAS UE Tune AU2-MSTW2008LO [51]. Reconstruction of small-radius jets (from hereon referred to just as ‘jets’) for the mono-jet channel is performed by FASTJET[63] using the anti- k_T algorithm with radius parameter $R = 0.4$. Similarly, reconstruction of large-radius jets for the mono- W/Z channel is performed using the Cambridge-Aachen algorithm with $R = 1.2$. The latter channel also includes a mass-drop filtering procedure with $\mu = 0.67$ and \sqrt{y} ⁶ = 0.4 (see ref. [62] for further details), which favours large- R jets with two balanced subjets, consistent with the decay of an EW boson to a (potentially-boosted) dijet pair. Lastly, the detector response is approximated by applying a Gaussian smearing factor to the p_T of all leptons and jets.

3.1.1 Parton Matching Scheme

In the ATLAS mono-jet analysis, matching of partons generated in MADGRAPH5 to jets generated in PYTHIA 8 is performed using the MLM scheme [61], with two matching scales, or values of ‘QCUT’, per mass/coupling point. The QCUT values span a broad kinematic range in combination with a cut placed on the leading jet p_T per event to avoid double-counting. This treatment aims to mitigate the impact of the matching scale on the shape of the p_T and E_T^{miss} distributions; that is, to reduce the uncertainty in those areas of phase space where the mediator mass is significantly larger or smaller than the QCUT value. For the analysis of SiMs, we use instead a single matching scale of 80 GeV. Though not ideal, this approach suitably reproduces the results of the ATLAS mono-jet analysis for the masses of interest (see Sec. B.1). Importantly, it also reduces the complexity and computational expense involved in estimating limits for the mono-jet channel.

We now move to a discussion of each of the mono- X channels separately.

3.2 Mono-jet Constraints

The ATLAS mono-jet + E_T^{miss} analysis [41] was originally designed to set limits on three new physics scenarios, the most relevant of which is the production of WIMP DM within

⁵Jets are seeded by any parton excluding the (anti-)top quark.

⁶ $\sqrt{y} = \min(p_{T_{j_1}}, p_{T_{j_2}})\Delta R/m_{jet}$ is the momentum balance of the two leading subjets.

the context of a set of effective operators. The analysis also includes a brief study of a Z' DM model which is analogous to our sV model.

Signal selection is carried out based on at least one hard jet recoiling against missing energy. To ensure that the correct back-to-back jet + E_T^{miss} topology is selected events are required to have a leading jet, j_1 , with $p_T > 120$ GeV and $|\eta| < 2.0$ satisfying $p_T^{j_1}/E_T^{\text{miss}} > 0.5$. Surviving events must then satisfy $|\Delta\phi(j, \vec{E}_T^{\text{miss}})| > 1.0$, where j is any jet with $p_T > 30$ GeV and $|\eta| < 4.5$. This criterion reduces the multijet background contribution where the large E_T^{miss} originates mainly from jet energy mismeasurement. Note that there is no upper limit placed on the number of jets per event. The contribution from the dominant background processes, W/Z +jets, is managed with a veto on events containing muons or electrons with $p_T > 7$ GeV. Lastly, nine separate signal regions are defined with increasing lower thresholds on E_T^{miss} , which range from 150 GeV to 700 GeV as shown in table 2.

The ATLAS mono-jet analysis revealed no significant deviation of observed events from the expected SM backgrounds in the Run 1 8 TeV dataset. Subsequently, model-independent limits on new physics signatures were provided in terms of the visible cross-section, $\sigma \times \mathcal{A} \times \epsilon$; these are listed in table 2.

| Signal Region | E_T^{miss} threshold [GeV] | $\sigma \times \mathcal{A} \times \epsilon$ [fb] |
|---------------|-------------------------------------|--------------------------------------------------|
| SR1 | 150 | 726 (935) |
| SR2 | 200 | 194 (271) |
| SR3 | 250 | 90 (106) |
| SR4 | 300 | 45 (51) |
| SR5 | 350 | 21 (29) |
| SR6 | 400 | 12 (17) |
| SR7 | 500 | 7.2 (7.2) |
| SR8 | 600 | 3.8 (3.2) |
| SR9 | 700 | 3.4 (1.8) |

Table 2: The ATLAS mono-jet E_T^{miss} signal regions and corresponding observed (expected) model-independent upper limits on $\sigma \times \mathcal{A} \times \epsilon$ at 95% confidence level. Adapted from Ref. [41].

The signal simulation procedure outlined in sec. 3.1 and implementation of the selection criteria discussed above were validated for the mono-jet channel via reproduction of ATLAS limits on the suppression scale, $M_\star \equiv M_{\text{med}}/\sqrt{g_q g_\chi}$, for the Z' model. The details of this process are contained in appendix B.1. Importantly, we observe agreement within $\sim 12\%$ for all samples.

3.3 Mono- Z Constraints

The ATLAS mono- $Z(\rightarrow \ell^+ \ell^-) + E_T^{\text{miss}}$ analysis [47] was principally designed to constrain a set of EFT models of DM. As a secondary focus, it also includes a short study of a t -channel simplified model similar to our tS model.

288 The selection criteria for this analysis are summarised as follows (see the paper for a
 289 full description). Electrons (muons) are required to have a p_T greater than 20 GeV, and
 290 $|\eta|$ less than 2.47 (2.5). Two opposite-sign, same-flavour leptons are selected, and required
 291 to have invariant mass and pseudorapidity such that $m_{\ell\ell} \in [76, 106]$ GeV and $|\eta^{\ell\ell}| < 2.5$.
 292 The reconstructed Z boson should be approximately back-to-back and balanced against
 293 the E_T^{miss} , ensured with the selections $\Delta\phi(\vec{E}_T^{\text{miss}}, p_T^{\ell\ell}) > 2.5$ and $|p_T^{\ell\ell} - E_T^{\text{miss}}|/p_T^{\ell\ell} < 0.5$.
 294 Events containing a jet with $p_T > 25$ GeV and $|\eta| < 2.5$ are vetoed. Events are also vetoed
 295 if they contain a third lepton with $p_T > 7$ GeV. The signal regions are defined by increasing
 296 lower E_T^{miss} thresholds: $E_T^{\text{miss}} > 150, 250, 350, 450$ GeV.

297 A cut-and-count strategy is used to estimate the total observed yields and expected SM
 298 backgrounds in each signal region. The limits on $\sigma \times \mathcal{A} \times \epsilon$ are not publicly available, so we
 299 take the numbers of expected and observed events, along with the associated uncertainties,
 300 and convert these into model-dependent upper limits with a single implementation of the
 301 HistFitter framework [54] using a frequentist calculator and a one-sided profile likelihood
 302 test statistic (the LHC default). The results of this process are displayed in table 3. Note
 303 that we use signal regions 1 and 2 only, as our simplified HistFitter approach is inadequate
 304 to handle the very low statistics of signal regions 3 and 4. These upper limits are also used
 305 for the validation of the mono- Z signal generation and selection procedures (see app. B.2).

| Signal Region | E_T^{miss} threshold [GeV] | $\sigma \times \mathcal{A} \times \epsilon$ [fb] |
|---------------|-------------------------------------|--------------------------------------------------|
| SR1 | 150 | 1.59 (1.71) |
| SR2 | 250 | 0.291 (0.335) |

Table 3: The ATLAS mono- Z E_T^{miss} signal regions and corresponding observed (expected) model-independent upper limits on $\sigma \times \mathcal{A} \times \epsilon$ at 95% confidence level. Adapted using HistFitter from ref. [47].

306 3.4 Mono- W/Z Constraints

307 The ATLAS mono- $W/Z + E_T^{\text{miss}}$ search [48] was aimed at constraining the spin-independent
 308 effective operators C1, D1, and D5, and the spin-dependent operator D9. The search
 309 was originally designed to exploit the constructive interference of W boson emission from
 310 opposite-sign up-type and down-type quarks, leading to DM production wherein the mono-
 311 W channel is dominant. Recent studies [64] have revealed this scenario to violate gauge
 312 invariance and so we ignore it in this analysis. (should we not add some motivation on why
 313 we include it? Millie, you commented out these parts, maybe you could pick your favourite
 314 sentence or so and put it back in, in case you agree?)

315 The mono- W/Z event selection is carried out as follows. Large-radius jets are selected
 316 using a mass-drop filtering procedure (see sec. 3.1) to suppress non- W/Z processes. Events
 317 are required to contain at least one large- R jet with $p_T > 250$ GeV, $|\eta| < 1.2$ and a mass,
 318 m_{jet} , within a 30-40 GeV window of the W/Z mass (i.e. $m_{\text{jet}} \in [50, 120]$ GeV). In order
 319 to reduce the $t\bar{t}$ and multijet backgrounds, a veto removes events containing a small- R jet

with $\Delta\phi(\text{jet}, E_T^{\text{miss}}) < 0.4$, or containing more than one small- R jet with $p_T > 40$ GeV, $|\eta| < 4.5$, and $\Delta R(\text{small-}R \text{ jet}, \text{large-}R \text{ jet}) > 0.9$. Electrons, muons and photons are vetoed if their p_T is larger than 10 GeV and they lie within $|\eta| < 2.47$ (electrons), 2.5 (muons), 2.37 (photons). Two signal regions were defined with $E_T^{\text{miss}} > 350$ GeV and $E_T^{\text{miss}} > 500$ GeV.

The ATLAS analysis used a shape-fit of the mass distribution of the large- R jet to estimate the background yields in the two signal regions, along with the associated statistical and systematic uncertainties. As in the mono- Z case, we do not take the shapes into account but convert the published number of expected and observed events into upper limits on the expected and observed number of new physics events using the HistFitter framework. For the $E_T^{\text{miss}} > 500$ GeV signal region, we obtain the limits shown in table 4. We do not consider the first signal region with $E_T^{\text{miss}} > 350$ GeV in the recasting procedure, since the cut-and-count limits extracted could not be convincingly validated. The high E_T^{miss} signal region was found to be optimal for most operators studied by the ATLAS analysis. (add that in other cases the two perform similar?)

| Signal Region | E_T^{miss} threshold [GeV] | $\sigma \times \mathcal{A} \times \epsilon$ [fb] |
|---------------|-------------------------------------|--------------------------------------------------|
| SR2 | 500 | 1.35 (1.34) |

Table 4: The ATLAS mono- W/Z E_T^{miss} signal region considered in this work and corresponding observed (expected) model-independent upper limits on $\sigma \times \mathcal{A} \times \epsilon$ at 95% confidence level. Adapted using HistFitter from ref. [48].

4 Results and Discussion

4.1 Limits on the coupling $\sqrt{g_q g_\chi}$

The 95% confidence level upper limits on the sV and sA model coupling combination $\sqrt{g_q g_\chi}$, and the tS model coupling $g_{q\chi}$, obtained from each of the mono- X channels, are presented in figs. 3-8. These quantities were evaluated as described in appendix A, including statistical and systematic uncertainties, and correspond to the best limits of each signal region tested.

In each plot, limits are shown ranging from <0.01 to the upper perturbative limit for each coupling, $4\pi^7$; where a limit was calculated to be larger than this, that limit is considered meaningless and the region is coloured grey. The white (hatched) regions coincide with those mass points which yield an initial (final) value of $\sqrt{g_q g_\chi}$ or $g_{q\chi}$ which fails to satisfy our requirement that $\Gamma < M_{\text{med}}/2$. (We observe that values for which the width is just within our upper validity bound of $M_{\text{med}}/2$ may be pushed over into the invalid range with the addition of new particles, not considered here, which would serve

⁷We note that perturbativity is questionable for couplings greater than $\sim 2 - 3$, however 4π is an oft-quoted hard upper limit.

to increase the mediator width.) When $g_\chi/g_q = 0.2$, only the mono-jet channel produces limits which survive this requirement, and so these are shown separately in fig. 7.

Detailed comments specific to each channel are below, however some trends are channel-independent. For the sV model, strong limits exist when $M_{\text{med}} > 2m_\chi$ as the mediator can go on-shell, thereby enhancing the cross-section. The sA model limits show similar behaviour to the sV model except in the region where $m_\chi \gtrsim 10 \times M_{\text{med}}$, where the cross-section is greatly enhanced **WHY?**. The upper limit on $\sqrt{g_q g_\chi}$ is relatively constant across values of g_χ/g_q , as is expected when the coupling (and hence the width) has been demonstrated to have little effect on kinematic behaviour, and using the assumptions of eq. 2.7. As the ratio increases, points in the region $M_{\text{med}} > m_\chi$ disappear as the initial condition, $g_q = 1$, leads to failure of the width condition. However, one could easily have chosen a smaller initial value of g_q to recover these points, and we suggest that the limits in this region would be quite similar to those seen in the $g_\chi/g_q = 0.2$ and 0.5 cases.

The results are limited when m_χ or M_{med} is large due to the smaller cross-sections in these cases, and are expected to improve at higher centre-of-mass energies. At small DM masses, the E_T^{miss} distribution peaks at low values (with the exception of the tS model in the mono-jet channel), so results in this region of phase space are limited by statistical uncertainties from being in the tail of the distribution; this region would benefit from further optimisation of event selection in analyses aimed at SiM study, as we expect to see from the upcoming Run II results.

The results are discussed according to channel below.

4.1.1 Mono-jet channel

The upper limits on the coupling combination $\sqrt{g_q g_\chi}$ of the sV and sA models, obtained in the mono-jet channel, are displayed in the left-hand column of figs. 3-6, for $g_q/g_\chi = 0.5, 1, 2$ and 5 respectively. Additional results for the $g_q/g_\chi = 0.2$ case are also shown separately in fig. 7, as these limits are only meaningful within this channel.

As expected, the mono-jet channel produces the strongest coupling limits in both s -channel models, which are better than those from the next-best mono- Z channel by a factor of a few. For the sV model, the weakest limits result for large m_χ or large M_{med} , and in fact are so weak that they are pushed into the region of invalidity where $\Gamma > M_{\text{med}}/2$; this is because although the acceptance is considerably higher in these regions compared to low masses, the cross section is sufficiently small that this effect prevails. Within the valid region ($m_\chi \in [1, 100]$ GeV and $M_{\text{med}} \in [1, 200]$ GeV), the limit on $\sqrt{g_q g_\chi}$ generally ranges from 0.1 to 0.7 , with a handful of on-shell masses reaching a limit of ~ 0.05 in the large g_χ/g_q case. In the large g_χ/g_q scenario, limits for $m_\chi = 1000$ GeV start to become valid. This is because if $\sqrt{g_q g_\chi}$ remains constant but the g_χ/g_q increases then the value of g_q is pushed downward and so the width, which is dominated by decays to SM particles, decreases.

The sA model displays similar behaviour to the sV model except for the $m_\chi \gtrsim 10 \times M_{\text{med}}$ region, as described above.

The uncertainties on the limits in the sV model generally range from ??% to ??%, and are dominated by **X**. The uncertainties for the sA model are dominated by **X** and are

391 within the range $X \sim Y\%$.

392 4.1.2 Mono- Z channel

393 The simplicity of the mono- Z channel relative to the mono-jet channel, and the speed of
 394 its production within MADGRAPH5, allowed us to study a finer granularity of points in the
 395 mass phase space. The resulting limits on the sV and sA models are shown in the central
 396 column of figs. 3-6. The behaviour of the limits as g_χ/g_q varies is similar to that within the
 397 mono-jet channel, and overall the limits are weaker compared to that channel by a factor
 398 of a few.

399 The total relative uncertainties on $\sqrt{g_q g_\chi}$ in the s -channel models are generally within
 400 10%, but can range up to 80% in a few cases; they are dominated by X.

401 The advantage of the mono-boson channels is in the study of the tS model; since this
 402 was not included in the mono-jet channel the strongest limits are obtained with the mono- Z
 403 analysis, and are shown in the left-hand side of fig. 8. Note that the scale here is increased
 404 by a factor of 10 from the s -channel model limits, in general the tS model limits are weaker
 405 than the corresponding s -channel points, thanks to an orders-of-magnitude weaker cross-
 406 section and the inability of the mediator to go on-shell in this channel. We find stronger
 407 limits for smaller m_χ and M_{med} masses, where larger cross sections compensate for lower
 408 acceptances at these points.

409 4.1.3 Mono- W/Z channel

410 The limits on the couplings of the sV , sA and tS models, obtained within the mono- W/Z
 411 channel, are shown in the right-hand column of figs. 3-8. This channel was studied to
 412 compare with the leptonic mono- Z channel in particular, but a coarser selection of masses
 413 was chosen as the limits were initially found to be somewhat weaker. Additionally, further
 414 estimates were made: a) as the kinematic behaviour is reasonable independent of the
 415 couplings, a single acceptance was found for each (m_χ, M_{med}) combination and applied to
 416 each value of g_χ/g_q , and b) complete systematic uncertainties were generated for a subset of
 417 masses and compared to those from the mono- Z channel; from this comparison the mono- Z
 418 systematic uncertainties were multiplied by 3 and then applied to the mono- W/Z limits. As
 419 a result, the limits obtained in this channel are not intended to be rigorously quantitative;
 420 rather, they are used more to indicate qualitatively how the channel compares.

421 The ATLAS mono- W/Z analysis (and in particular the higher E_T^{miss} signal region) was
 422 not optimised for a simplified model interpretation, and much of the phase space produced
 423 insignificant numbers of events passing the event selection, with up to 200 thousand events
 424 generated. Generally, the limits are a factor of a few weaker again than those from the
 425 mono- Z channel, which is both consistent with the limits on the EFT models studied in
 426 the ATLAS analyses, and expected following our use of a cut-and-count interpretation of
 427 the mono- W/Z public results (can we say this? Point is to compare with them probably
 428 doing a shape analysis to improve their limits).

429 In some cases - most notably the $m_\chi \gtrsim 10 \times M_{\text{med}}$ region - the limits become comparable
 430 with the mono- Z channel, suggesting that more statistics and an improved treatment of
 431 systematic uncertainties would bring these closer in line with that channel.

Overall, the uncertainties from this channel lie within the range XXX and are dominated by Y.

4.2 Comparison with Relic Density Constraints

In Figs. ?? we show lines where the constraint on the coupling corresponds to the coupling strength that would reproduce the correct DM density if DM is a thermal relic of the early universe. For points diagonally above and to the left of the dashed line, the LHC constraints naively rule out the couplings leading to the correct relic density. Below and to the right of this line the relic density coupling is still allowed.

In this scenario, the measured abundance is approximately related to the unknown self-annihilation cross-section via

$$\Omega_{\text{DM}} h^2 \simeq \frac{2 \times 2.4 \times 10^{-10} \text{ GeV}^{-2}}{\langle \sigma v \rangle_{\text{ann}}}. \quad (4.1)$$

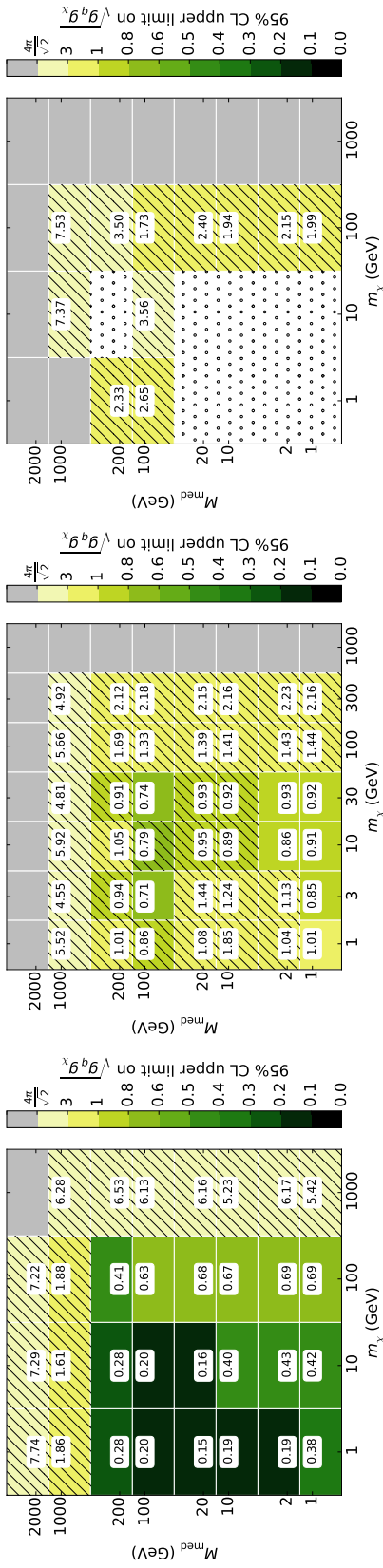
This is used with measurements of the DM abundance by Planck, $\Omega_{\text{DM}}^{\text{obs}} h^2 = 0.1199 \pm 0.0027$ [36], to find $\langle \sigma v \rangle_{\text{ann}} \simeq 4.0 \times 10^{-9} \text{ GeV}^{-2}$ for thermal relic DM. This relation is only approximately accurate, and so we use the Micromegas code [52] to determine the coupling strength leading to the correct relic density for each model. We verified this technique against the semi-analytic technique outlined in e.g. Ref. [37].

If the DM mass lies at the electroweak scale, the thermal relic scenario provides a natural explanation for the observed DM density, and so the coupling strengths leading to the correct relic density are a natural benchmark with which to compare constraints from other DM searches, indicating the scale at which we expect the couplings may lie. However the relic density couplings should by no means be treated as a constraint. If the DM was not produced thermally or if there is some unknown effect which modifies the evolution of the density with temperature, then these relations break down. Further, even if DM is a thermal relic, then the relationship no longer holds if there are other annihilation channels not taken into account, or if there are other beyond-SM particles contributing to the DM abundance.

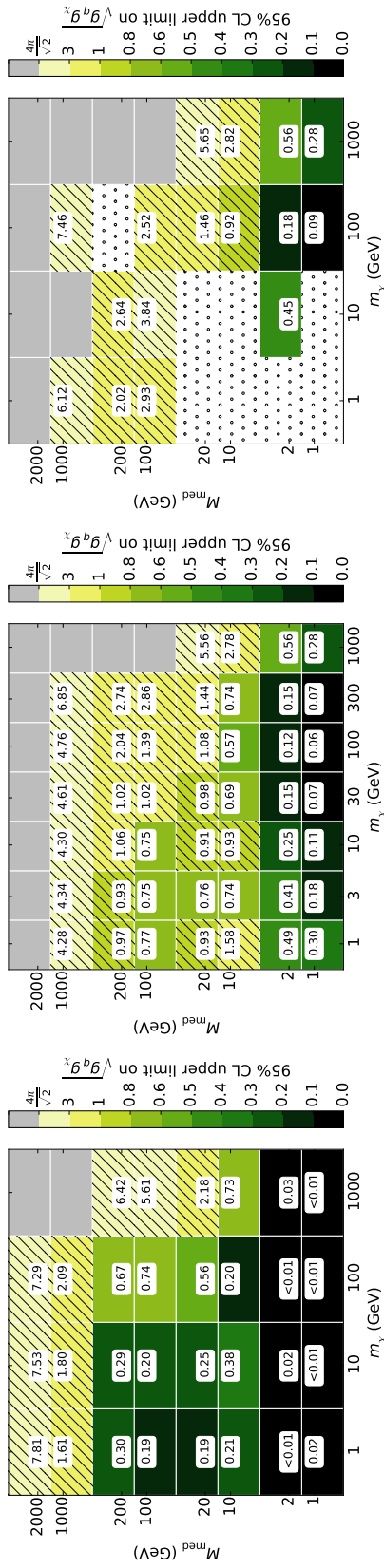
4.3 Comparison with Direct Detection Constraints

In Figs. ?? we also show the intercept line where constraints from direct detection experiments are equally as strong as the LHC constraint. Below and to the right of the dotted line, direct detection constraints are stronger than the LHC constraint, while above and to the left, the LHC gives the stronger constraint. We use the toolset from Ref. [?] to convert the strongest available direct detection constraints, which are from the LUX 2013 dataset [?], onto constraints on our models.

Compared to direct detection, the LHC performs relatively better for the SAD model than for the SVD model. This is because the axial-vector coupling leads to a suppressed scattering rate in direct detection experiments while the LHC is relatively insensitive to the difference between the vector and axial-vector couplings. In the non-relativistic limit, the TSD model leads to a mix of both suppressed and unsuppressed operators.

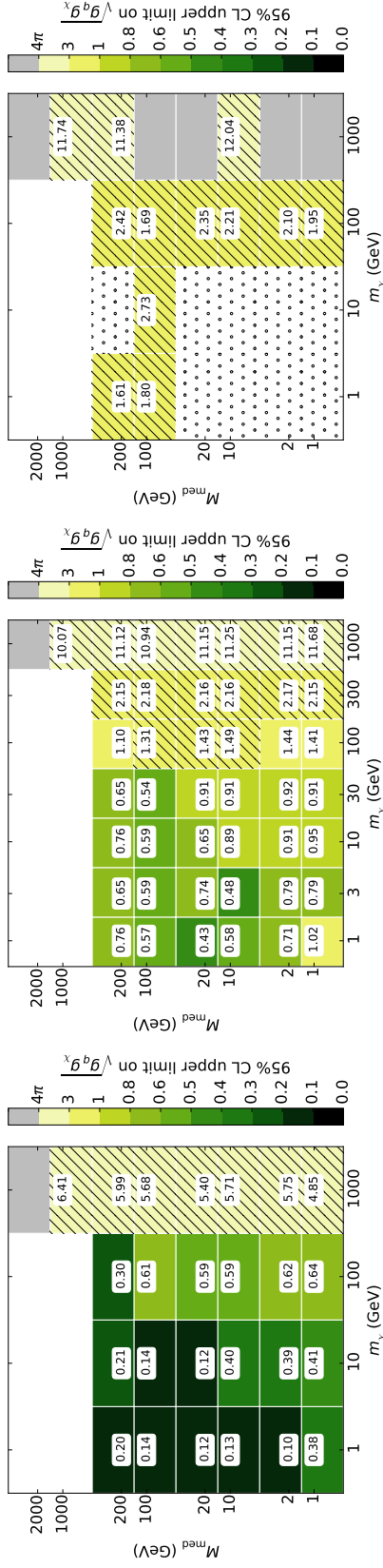


(a) sV model, $g_q/g_\chi = 0.5$, mono-jet channel. (b) sV model, $g_q/g_\chi = 0.5$, mono-Z channel. (c) sV model, $g_q/g_\chi = 0.5$, mono- W/Z channel.

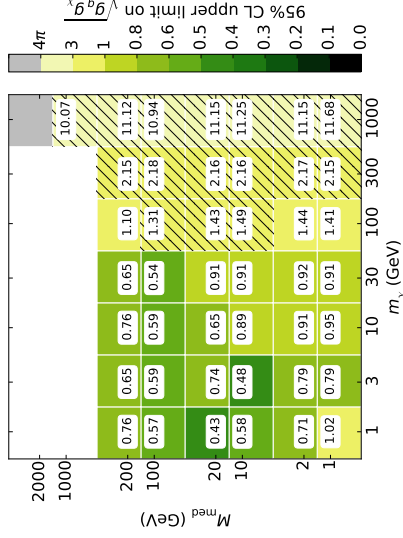


(d) sA model, $g_q/g_\chi = 0.5$, mono-jet channel. (e) sA model, $g_q/g_\chi = 0.5$, mono-Z channel. (f) sA model, $g_q/g_\chi = 0.5$, mono- W/Z channel.

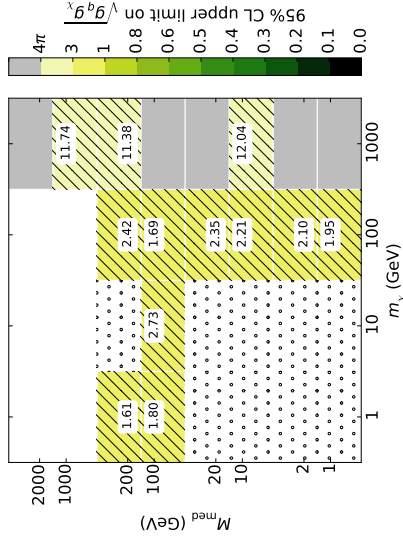
Figure 3: Upper limits on the coupling for the s -channel models in the mono-jet (left), mono-Z (centre) and mono- W/Z (right) channels, for $g_\chi/g_q = 0.5$. The grey region represents the phase space where no meaningful limit was obtained. The hatched region represents a limit which leads to a width greater than $M_{\text{med}}/2$, so the validity of the calculation begins to fail. The dotted region represents phase space where insufficient statistics were available.



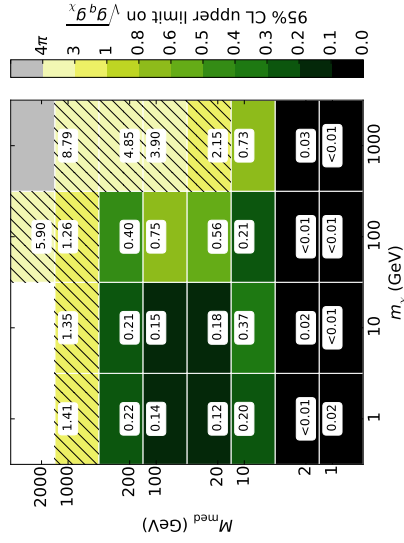
(a) sV model, $g_q/g_\chi = 1$, mono-jet channel.



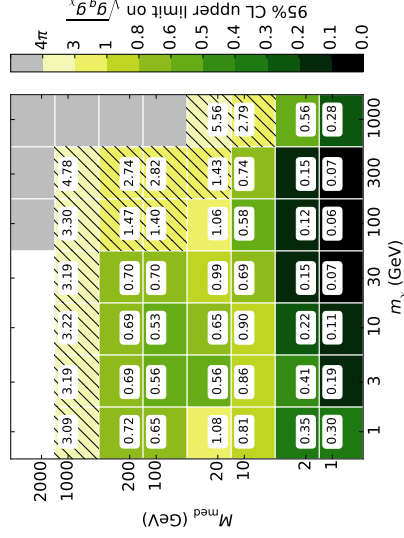
(b) sV model, $g_q/g_\chi = 1$, mono-Z channel.



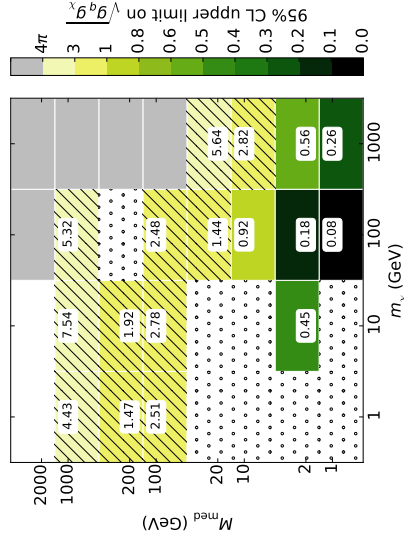
(c) sV model, $g_q/g_\chi = 1$, mono-W/Z channel.



(d) sA model, $g_q/g_\chi = 1$, mono-jet channel.



(e) sA model, $g_q/g_\chi = 1$, mono-Z channel.



(f) sA model, $g_q/g_\chi = 1$, mono-W/Z channel.

Figure 4: Upper limits on the couplings for the s-channel models in the mono-jet (left), mono-Z (centre) and mono-W/Z (right) channels, for $g_\chi/g_q = 1$. Refer to fig. 3 for details.

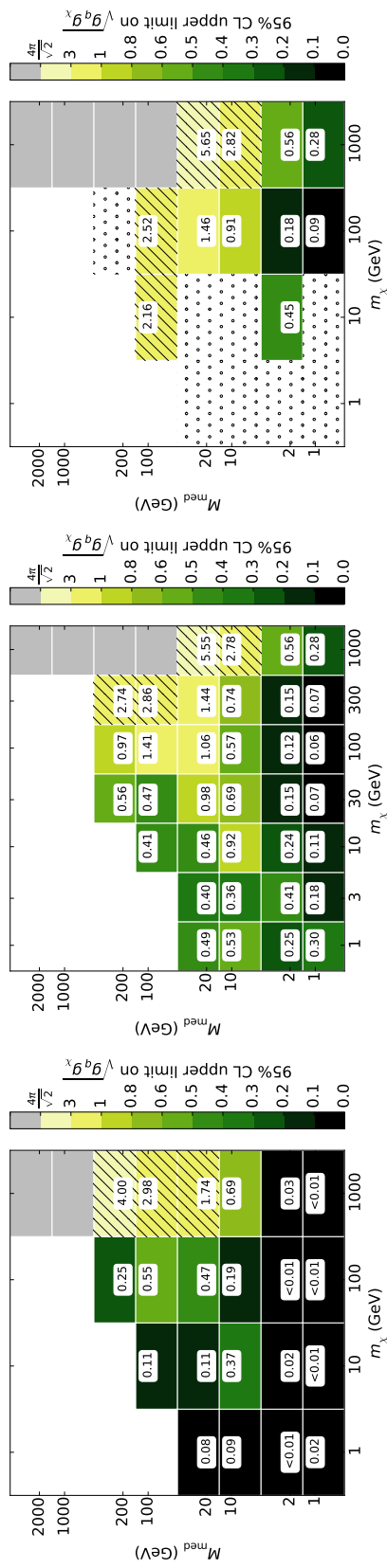
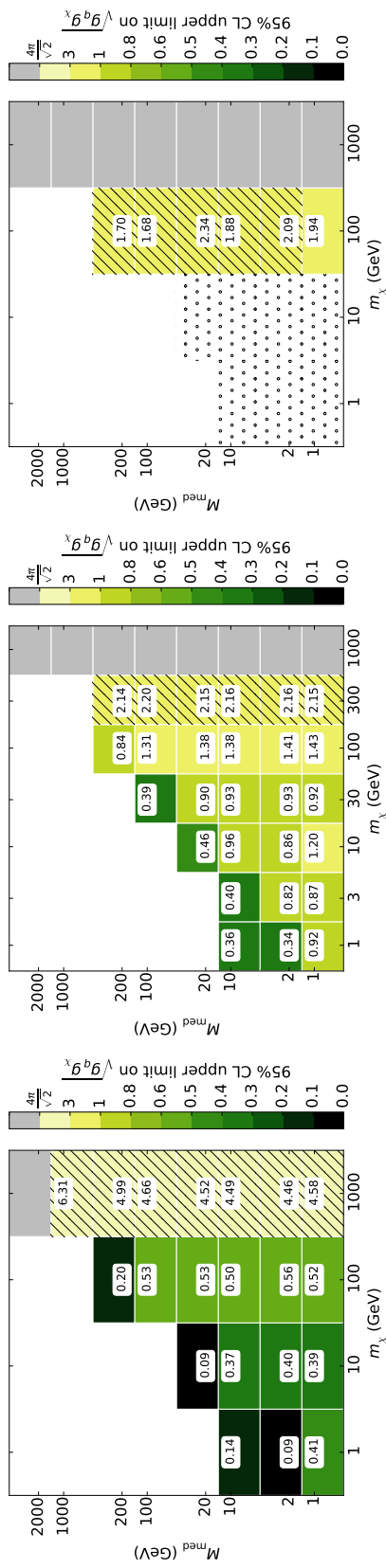
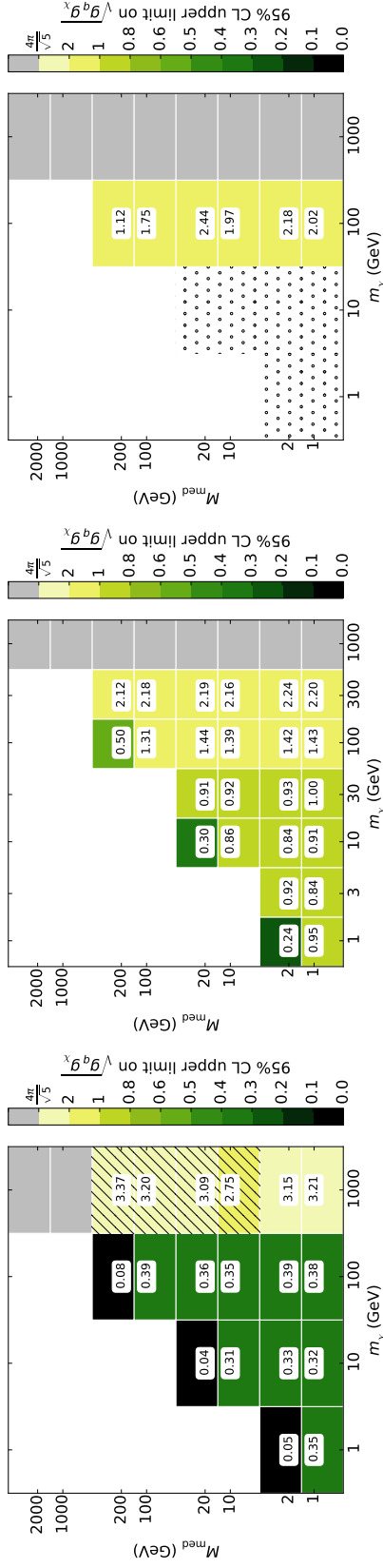
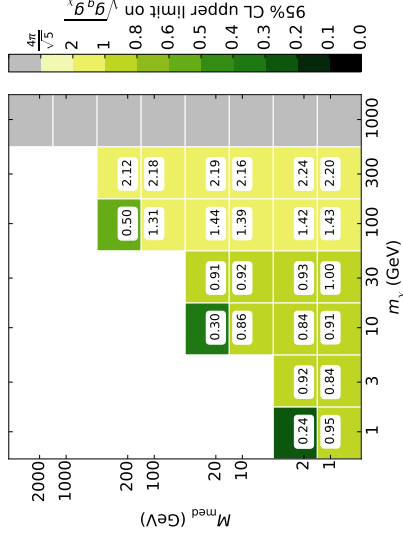


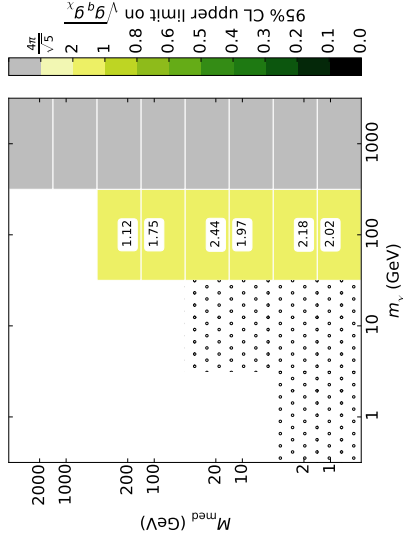
Figure 5: Upper limits on the coupling for the s-channel models in the mono-jet (left), mono-Z (centre) and mono- W/Z (right) channels, for $g_\chi/g_q = 2$. Refer to fig. 3 for details.



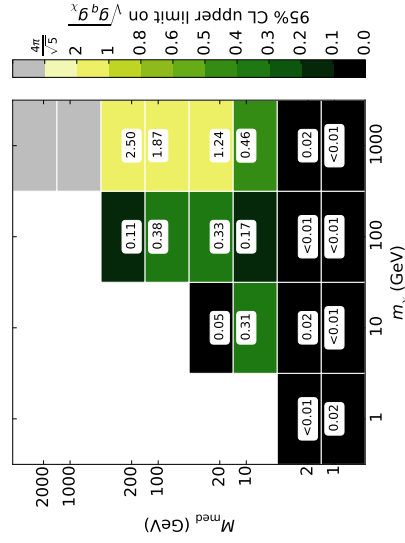
(a) sV model, $g_q/g_\chi = 5$, mono-jet channel.



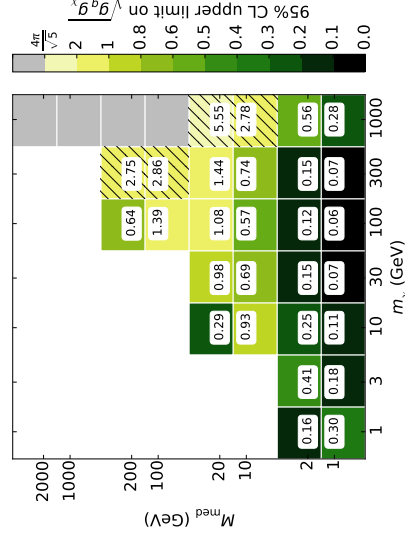
(b) sV model, $g_q/g_\chi = 5$, mono- Z channel.



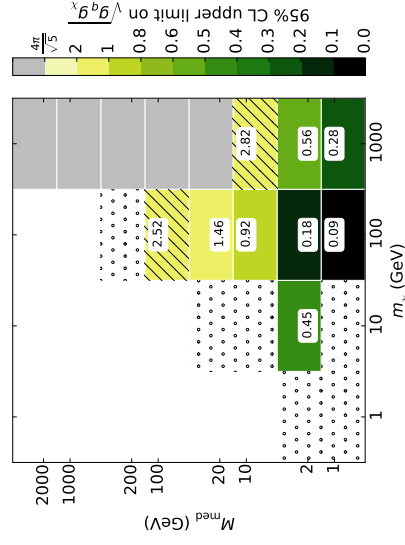
(c) sV model, $g_q/g_\chi = 5$, mono- W/Z channel.



(d) sA model, $g_q/g_\chi = 5$, mono-jet channel.



(e) sA model, $g_q/g_\chi = 5$, mono- Z channel.



(f) sA model, $g_q/g_\chi = 5$, mono- W/Z channel.

Figure 6: Upper limits on the coupling for the s -channel models in the mono-jet (left), mono- Z (centre) and mono- W/Z (right) channels, for $g_\chi/g_q = 5$. Refer to fig. 3 for details.

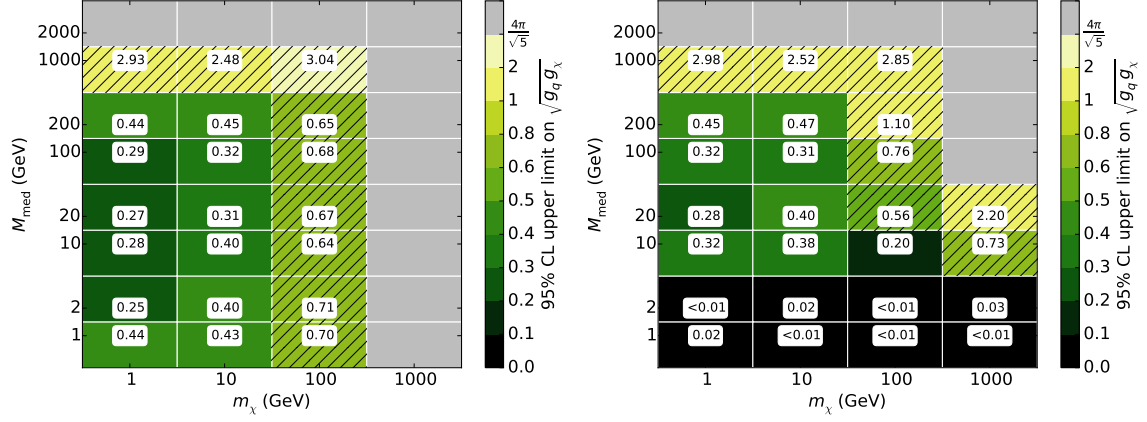


Figure 7: Upper limits on the coupling for the s -channel models in the mono-jet channel, for $g_\chi/g_q = 0.2$. Refer to fig. 3 for details.

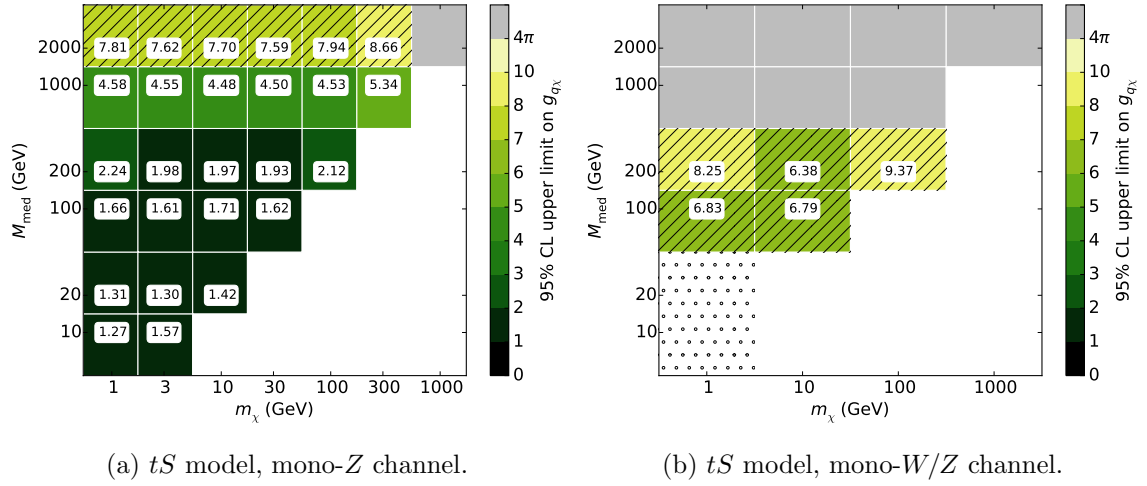


Figure 8: Upper limits on the coupling $g_{q\chi}$ for the t -channel model in the mono- Z (left) and mono- W/Z (right) channels. Refer to fig. 3 for details.

The direct detection constraints assume that the DM candidate under consideration contributes 100% of the local DM density, while the LHC constraints make no assumptions about either the local DM density or overall abundance. In this sense the LHC constraints remain useful even in the region where they are not as strong as those from direct detection.

4.4 Discussion

- Comparison to direct mediator searches: dijet gives strongest constraints on mediator especially for small r . Missing ET still good for large M but in this region EFT is fine
- Comparison to non-grid searches, e.g. McCullough et al
- Comparison to grid searches e.g. Zurek et al, Jacques and Nordstrom

5 Conclusion

MonoX searches dominate.

6 Acknowledgements

A Limit setting strategy

In this appendix we present a summary of the procedure employed to calculate the 95% confidence level (CL) limits on the coupling parameter $\sqrt{g_q g_\chi}$, where this parameter can be replaced with $g_{q\chi}$ for the tS model, and M_\star in the validation of the mono-jet analysis.

A.1 Nominal Values

For each SiM, the nominal limit is calculated by taking the model-independent upper limit on $\sigma \times \mathcal{A} \times \epsilon$ from each analysis, dividing by the value of $\mathcal{A} \times \epsilon$ (which is taken as a single parameter for each point) to obtain the limiting cross section σ_{lim} , and rearranging eq. 2.7 to convert to a limit on the couplings. In the s -channel, on-shell case, the width can be expressed as a function of g_q and the ratio g_χ/g_q , which simplifies the calculation. We arrive at

$$\sqrt{g_q g_{\chi_{\text{lim}}}} = \begin{cases} \sqrt{g_q g_{\chi_{\text{gen}}}} \times (\sigma_{\text{lim}}/\sigma_{\text{gen}})^{\frac{1}{2}} & \text{if } M_{\text{med}} \geq 2m_{\text{DM}} \text{ (} s\text{-channel)} \\ \sqrt{g_q g_{\chi_{\text{gen}}}} \times (\sigma_{\text{lim}}/\sigma_{\text{gen}})^{\frac{1}{4}} & \text{if } M_{\text{med}} < 2m_{\text{DM}} \end{cases} \quad (\text{A.1})$$

where $\sqrt{g_q g_{\chi_{\text{gen}}}}$ and σ_{gen} are the input couplings and resulting cross-section (taken from PYTHIA 8), respectively.

The signal region in each case is chosen based on where the best ‘expected’ limit exists, where that limit is calculated assuming that exactly the expected SM background is observed.

| main systematic sources | PDF/tune | factorisation and renormalisation scales | matching scale (mono-jet only) |
|-------------------------|---------------------------------------------|------------------------------------------|--------------------------------|
| variation ‘up’ | NNPDF2.1LO + Monash tune | 2 | 160 GeV |
| nominal | MSTW2008lo68cl + ATLAS UE AU2-MSTW2008LO | 1 | 80 GeV |
| variation ‘down’ | CTEQ6L1 + ATLAS UE AU2-CTEQ6L1 | 0.5 | 40 GeV |

Table 5: The sources of systematic uncertainty considered in this analysis. Each point in phase space is varied up or down by one of these sources, and the systematic uncertainty is taken to be the average difference in modified acceptance from the nominal value.

A.2 Uncertainty Estimation

Our nominal limits rely on both σ_{gen} and $\mathcal{A} \times \epsilon$ and so are subject to systematic uncertainties which derive from our choice of MC generation procedure. For our MC samples, there are three key sources of systematic uncertainty: the factorisation and renormalisation scales, the strong coupling constant (α_s) and the choice of parton distribution function (PDF). Should we say something about the actual choice of generator here? And what about LO vs NLO?)

The factorisation and renormalisation default scales are straightforward to test in MADGRAPH5 where they varied simultaneously by factors of 2 (‘up’) and 0.5 (‘down’). The systematic effects of the strong coupling constant and the PDF are difficult to separate and so are treated in tandem. We assume that the systematic uncertainty introduced by α_s at matrix-element level is negligible when compared to the PDF uncertainties, as demonstrated to be valid in ref. [42]. The variation of α_s in conjunction with a PDF is done with the use of specific tunes in PYTHIA 8, which we change simultaneously with the PDF choice to estimate the uncertainty on $\Delta\sigma_{gen}$. The nominal choices of PDF and tune are varied ‘up’ to NNPDF2.1LO PDF + Monash tune, and ‘down’ to CTEQ6L1 PDF and ATLAS UE AU2-CTEQ6L1 tune. Millie: put discussion of matching scale systematic here. These systematic uncertainty sources are summarised in table 5.

The average variation from the nominal value of σ_{lim} , as a fraction of σ_{lim} , resulting from each systematic source is added in quadrature and propagated to $\sqrt{g_q g_\chi}$ to obtain the total systematic uncertainty. This process is adjusted slightly to account for the inclusion of statistical uncertainties, which are estimated rather conservatively by taking the 95% CL lower limit on $\mathcal{A} \times \epsilon$ as calculated with the Wald approximation, i.e. $\mathcal{A} \times \epsilon \rightarrow (\mathcal{A} \times \epsilon) - \Delta(\mathcal{A} \times \epsilon)$. The uncertainty on the luminosity is less than 3%, so is considered to be

negligible in comparison to other systematic sources.

B Validation of signal simulation and event selection procedures

B.1 Monojet Channel

The MC generation and signal selection procedures for the mono-jet channel are validated via reproduction of the ATLAS limits on $M_\star \equiv M_{\text{med}}/\sqrt{g_q g_\chi}$, for the s -channel vector simplified model. A comparison of SR7 limits for a representative sample of mediator masses with $m_\chi = 50$ GeV, $\Gamma = M/8\pi$ and $\sqrt{g_q g_\chi} = 1$ is presented in table 6. In general, good agreement is observed between the ATLAS and reproduced limits, with a maximum difference (with respect to the ATLAS limit) of $<23\%$. We note that a discrepancy such as this is expected and allowed for three reasons. Firstly, the MC generation procedure employed in this analysis does not include a full simulation of the ATLAS detector. Instead, reconstruction effects are simulated by applying a Gaussian smearing of the jet p_T . Secondly, the matching procedure employed in this analysis (and discussed in detail in Section 3.1.1) is largely simplified. This introduces a substantial uncertainty when compared to the matching procedure utilised by the ATLAS mono-jet group. For example, where the ATLAS group observe a maximum matching scale uncertainty of 5% for events with E_T^{miss} above 350 GeV, we observe an uncertainty of $\sim 30\%$. Lastly, the 95% CL uncertainties on M_\star for this work are estimated as described in appendix A, while the ATLAS analysis used a more complex HistFitter treatment (confirm). As our results are consistently more conservative than those of the ATLAS analysis, we consider this approach acceptable.

| M [TeV] | M_\star^{95} [GeV] (ATLAS) | M_\star^{95} [GeV] (this work) | Difference [%] |
|--------------|---------------------------------|-------------------------------------|-------------------|
| 0.05 | 91 | 89 | 2.16 |
| 0.3 | 1151 | 1041 | 7.3 |
| 0.6 | 1868 | 1535 | 11.8 |
| 1 | 2225 | 1732 | 12.0 |
| 3 | 1349 | 1072 | 6.8 |
| 6 | 945 | 769 | 8.5 |
| 10 | 928 | 724 | 10.6 |
| 30 | 914 | 722 | 9.6 |

Table 6: Comparison of the 95% CL upper limits on M_\star from this work and from the ATLAS mono-jet analysis [41]. The limits are compared for an s -channel model with $m_\chi = 50$ GeV and Γ set to a fixed width of $M_{\text{med}}/8\pi$, for the process $pp \rightarrow \chi\bar{\chi} + 1, 2j$ with QCUT = 80 GeV.

B.2 Mono-Z Channel

The ATLAS mono- Z analysis result includes an upper limit on the coupling $g_{q\chi}$ for a t -channel simplified model that is very similar to the tS model investigated here, and so

| m_χ [GeV] | M_{med} [GeV] | $g_{q\chi}^{95\% \text{CL}}$ (ATLAS) | $g_{q\chi}^{95\% \text{CL}}$ (this work) | Difference [%] |
|-------------------|---------------------------|-----------------------------------------|---------------------------------------------|-------------------|
| 10 | 200 | 1.9 | 2.0 | 5.3 |
| | 500 | 2.8 | 3.2 | 14.3 |
| | 700 | 3.5 | 4.4 | 25.7 |
| | 1000 | 4.5 | 5.2 | 15.6 |
| 200 | 500 | 3.4 | 4.0 | 17.6 |
| | 700 | 4.2 | 4.5 | 7.1 |
| | 1000 | 5.2 | 5.3 | 1.9 |
| 400 | 500 | 5.5 | 5.7 | 3.6 |
| | 700 | 6.1 | 6.5 | 6.6 |
| | 1000 | 7.2 | 7.4 | 2.8 |
| 1000 | 1200 | 23.3 | 24.1 | 3.4 |

Table 7: Comparison of the upper limit on $g_{q\chi}$ from the ATLAS analysis [47] and this work.

is used for validating our signal generation and selection procedure. The most significant differences are in the number of mediating particles — the ATLAS model includes just two mediators (*up*- and *down*-type) compared to our six — and in the nature of the DM particle, which is taken to be Majorana. Additionally, while we use a universal coupling $g_{q\chi}$ to all three quark generations, the analysis used a model which set $g_{t,b\chi} = 0$.

Table 7 shows the 95% CL upper limits on $g_{q\chi}$ that we calculate using the same t -channel model and our own generation procedure (using the values in table 3), compared with the limits on this same variable taken from the ATLAS analysis. The difference as a percentage of the ATLAS limit is also shown in the table. We see reasonable agreement; most of the 11 points in parameter space are within 10% of the ATLAS limits, and all are within 26%. Additionally, our results are consistently more conservative, which is to be expected due to the less sophisticated nature of our generation procedure. Similarly to the mono-jet validation, the dominant effects are due to the use of p_T smearing applied to the leptons, rather than considering the full reconstruction effects, and the simplified treatment of systematics; we also obtained $\sigma \times \mathcal{A} \times \epsilon$ independently.

B.3 Mono-W/Z Channel

The signal generation and event selection for the mono- W/Z channel are validated by reproducing the published limit on M_\star for the D5 EFT operator with $m_\chi = 1$ GeV. We see agreement within 12.5%, where our limit is slightly more conservative. This is to be expected for the following reasons: the D5 limits are only published for the low- E_T^{miss} signal region, whereas we use only the high- E_T^{miss} signal region in this recast; the ATLAS analysis uses a shape fit to extract the limit on the number of new physics events, whereas we

| m_χ [GeV] | $M_\star^{90\%CL}$ [GeV] (ATLAS) | $M_\star^{95\%CL}$ [GeV] (this work) | Difference [%] |
|-------------------|-------------------------------------|-----------------------------------------|-------------------|
| 1 | 570 | 499 | 12.5 |

Table 8: Comparison of the upper limit on M_\star from the ATLAS mono- W/Z analysis [48] and this work.

use a cut-and-count approach; and the ATLAS limit is quoted at 90% CL, while ours is calculated at 95% CL.

References

- [1] ATLAS Collaboration, *Search for new phenomena with the monojet and missing transverse momentum signature using the ATLAS detector in $\sqrt{s} = 7$ TeV proton-proton collisions*, *Phys. Lett. B* (2011), arXiv:1106.5327.
- [2] ATLAS Collaboration, *Search for New Phenomena in Monojet plus Missing Transverse Momentum Final States using 10 fb^{-1} of pp collisions at $\sqrt{s}=8$ TeV with the ATLAS detector at the LHC*, 2012, ATLAS-CONF-2012-147.
- [3] CMS Collaboration, *Search for new physics in monojet events in pp collisions at $\sqrt{s} = 8$ TeV*, 2013, CMS-PAS-EXO-12-048.
- [4] M. R. Buckley, *Using Effective Operators to Understand CoGeNT and CDMS-Si*, *Phys.Rev. D* 88, 055028 (2013), arXiv:1308.4146.
- [5] J. Abdallah et al., *Search for new phenomena with mono-jet plus missing transverse energy signature in pp collisions at $\sqrt{s}=8$ TeV with the ATLAS detector*, 2012, ATL-COM-PHYS-2012-1211.
- [6] N. Bell et al., *Searching for Dark Matter at the LHC with a Mono-Z*, *Phys.Rev. D* 86, 096011 (2012), arXiv:1209.0231.
- [7] N. Zhou, D. Berge, and D. Whiteson, *Mono-everything: combined limits on dark matter production at colliders from multiple final states*, *Phys.Rev. D* 87, 095013 (2013), arXiv:1302.3619.
- [8] M. Cahill-Rowley et al., *Complementarity and Searches for Dark Matter in the $pMSSM$* , SLAC-PUB-15450 (2013), arXiv:1305.6921.
- [9] ATLAS Collaboration, *Further search for supersymmetry at $\sqrt{s} = 7$ TeV in final states with jets, missing transverse momentum and isolated leptons with the ATLAS detector*, *Phys.Rev. D* 86, 092002 (2012), arXiv:1208.4688.
- [10] ATLAS Collaboration, *Search for squarks and gluinos with the ATLAS detector in final states with jets and missing transverse momentum using 4.7 fb^{-1} of $\sqrt{s} = 7$ TeV proton-proton collision data*, *Phys.Rev. D* 87, 012008 (2013), arXiv:1208.0949.
- [11] ATLAS Collaboration, *Search for pair-produced third-generation squarks decaying via charm quarks or in compressed supersymmetric scenarios in pp collisions at $\sqrt{s} = 8$ TeV with the ATLAS detector*, *Phys.Rev. D* 90, 052008 (2014), arXiv:1407.0608.

- [12] ATLAS Collaboration, *Search for squarks and gluinos with the ATLAS detector in final states with jets and missing transverse momentum using $\sqrt{s} = 8$ TeV proton-proton collision data*, *JHEP* 09 (2014) 146, arXiv:1405.7875.
- [13] H. Dreiner et al., *Contact Interactions Probe Effective Dark Matter Models at the LHC*, *Europhys.Lett.* (2013), arXiv:1303.3348.
- [14] J. Goodman et al., *Gamma Ray Line Constraints on Effective Theories of Dark Matter*, *Nucl.Phys.* (2011), arXiv:1009.0008.
- [15] G. Busoni et al., *On the Validity of the Effective Field Theory for Dark Matter Searches at the LHC*, *Phys.Lett.* (2014), arXiv:1307.2253.
- [16] G. Busoni et al., *On the Validity of the Effective Field Theory for Dark Matter Searches at the LHC, Part II: Complete Analysis for the s-channel*, *JCAP* 1406:060 (2014), arXiv:1402.1275.
- [17] G. Busoni et al., *On the Validity of the Effective Field Theory for Dark Matter Searches at the LHC Part III: Analysis for the t-channel*, *JCAP* 09 (2014) 022, arXiv:1405.3101.
- [18] Oliver Buchmueller, Matthew J. Dolan, Sarah A. Malik and Christopher McCabe, *Characterising dark matter searches at colliders and direct detection experiments: Vector mediators*, 2014, arXiv:1407.8257.
- [19] J. Kumar and D. Marfatia, *Matrix element analyses of dark matter scattering and annihilation*, *Phys.Rev.* (2013), arXiv:1305.1611.
- [20] G. Jungman et al., *Supersymmetric dark matter*, *Phys.Rept.* (1996).
- [21] P. J. Fox et al., *Missing Energy Signatures of Dark Matter at the LHC*, *Phys.Rev.* (2012), arXiv:1109.4398.
- [22] P. J. Fox, R. Harnik, R. Primulando, and C-T. Yu, *Taking a Razor to Dark Matter Parameter Space at the LHC*, *Phys.Rev.* (2012), arXiv:1203.1662.
- [23] M. Papucci, A. Vichi, and K. M. Zurek, *Monojet versus rest of the world I: t-channel Models*, *JHEP* (2014), arXiv:1402.2285.
- [24] Y. Bai, P. J. Fox, and R. Harnik, *The Tevatron at the Frontier of Dark Matter Direct Detection*, *JHEP* (2010), arXiv:1005.3797.
- [25] J. Goodman et al., *Constraints on Dark Matter from Colliders*, *Phys.Rev. D* 82, 116010 (2010), arXiv:1008.1783.
- [26] P. J. Fox, R. Harnik, J. Kopp, and Y. Tsai, *LEP Shines Light on Dark Matter*, *Phys.Rev.* (2011), arXiv:1103.0240.
- [27] M. L. Graesser, I. M. Shoemaker, and L. Vecchi, *A Dark Force for Baryons*, 2011, arXiv:1107.2666.
- [28] H. An and F. Gao, *Fitting CoGeNT Modulation with an Inelastic, Isopin-Violating Z' Model*, 2011, arXiv:1108.3943.
- [29] CMS Collaboration, *Search for narrow resonances using the dijet mass spectrum in pp collisions at $\sqrt{s} = 8$ TeV*, *Phys.Rev.* (2013), arXiv:1302.4794.
- [30] ATLAS Collaboration, *Search for high-mass resonances decaying to dilepton final states in pp collisions at $\sqrt{s} = 7$ -TeV with the ATLAS detector*, *JHEP* (2012), arXiv:1209.2535.

- [31] P. Harris, V. V. Khoze, M. Spannowsky and C. Williams, *Constraining Dark Sectors at Colliders: Beyond the Effective Theory Approach*, *Phys.Rev.* (2015), arXiv:1411.0535.
- [32] CMS Collaboration. *Search for new physics in monojet events in pp collisions at $\sqrt{s} = 8$ TeV*, 2013, CMS-PAS-EXO-12-048.
- [33] ATLAS Collaboration. *Search for New Phenomena in Monojet plus Missing Transverse Momentum Final States using 10 fb¹ of pp collisions at $\sqrt{s} = 8$ TeV with the ATLAS detector at the LHC*, 2012, ATLAS-CONF-2012-147.
- [34] J. Kumar and D. Marfatia, *Matrix element analyses of dark matter scattering and annihilation*, *Phys.Rev.* (2013), arXiv:1305.1611.
- [35] D. Alves et al., *Simplified Models for LHC New Physics Searches*, *J.Phys.* (2012), arXiv:1105.2838.
- [36] P. A. R. Ade *et al.* [Planck Collaboration], *Astron. Astrophys.* **571**, A16 (2014) [arXiv:1303.5076 [astro-ph.CO]].
- [37] G. Busoni, A. De Simone, T. Jacques, E. Morgante and A. Riotto, *Making the Most of the Relic Density for Dark Matter Searches at the LHC 14 TeV Run*, *JCAP* 03 (2015) 022, arXiv:1410.7409.
- [38] CMS Collaboration. *Search for new physics in monojet events in pp collisions at $\sqrt{s} = 8$ TeV*, 2013, CMS-PAS-EXO-12-048.
- [39] ATLAS Collaboration. *Search for New Phenomena in Monojet plus Missing Transverse Momentum Final States using 10 fb¹ of pp collisions at $\sqrt{s} = 8$ TeV with the ATLAS detector at the LHC*, 2012, ATLAS-CONF-2012-147.
- [40] ATLAS Collaboration. *Further search for supersymmetry at $\sqrt{s} = 7$ TeV in final states with jets, missing transverse momentum and isolated leptons with the ATLAS detector*, *Phys.Rev.* (2012), arXiv:1208.4688.
- [41] ATLAS Collaboration. *Search for new phenomena in final states with an energetic jet and large missing transverse momentum in pp collisions at $\sqrt{s} = 8$ TeV with the ATLAS detector*, 2015, arXiv:1502.01518
- [42] S. Schramm, *Searching for Dark Matter with the ATLAS Detector in Events with an Energetic Jet and Large Missing Transverse Momentum*, 2015, CERN-THESIS-2015-038.
- [43] A. Cooper-Sarkar. *PDFs for the LHC*, 2011, arXiv:1107.5170.
- [44] ATLAS Collaboration. *Search for dark matter candidates and large extra dimensions in events with a jet and missing transverse momentum with the ATLAS detector*, 2013, CERN-PH-EP-2012-210, arXiv:1210.4491.
- [45] P. J. Fox et al. *Missing Energy Signatures of Dark Matter at the LHC*, *Phys. Rev.*, 2012.
- [46] N. Bell, J. Dent, T. Jacques, and T. Weiler. *W/Z Bremsstrahlung as the Dominant Annihilation Channel for Dark Matter*, *Phys. Rev.*, 2011.
- [47] ATLAS Collaboration. *Search for dark matter in events with a Z boson and missing transverse momentum in pp collisions at $\sqrt{s} = 8$ TeV with the ATLAS detector*, *Phys.Rev.D* **90** (2014) 012004, arXiv:1404.0051.
- [48] ATLAS Collaboration. *Search for dark matter in events with a hadronically decaying W or Z boson and missing transverse momentum in pp collisions at $\sqrt{s} = 8$ TeV with the ATLAS detector*, *Phys. Rev. Lett.* **112** (2014) 041802, arXiv:1309.4017.

- [49] J. Alwall /emphet al.. *The automated computation of tree-level and next-to-leading order differential cross sections, and their matching to parton shower simulations*, *JHEP*07 (2014) 079, arXiv:1405.0301.
- [50] A. D. Martin, W. J. Stirling, R. S. Thorne, G. Watt, *Parton distributions for the LHC*, *Eur.Phys.J.C*63, (2009), 189-285, arXiv:0901.0002.
- [51] ATLAS Collaboration. *Summary of ATLAS Pythia8 tunes*, 2012, ATL-PHYS-PUB-2012-003.
- [52] G. Blanger, F. Boudjema, A. Pukhov and A. Semenov, *Comput. Phys. Commun.* **192**, 322 (2015) doi:10.1016/j.cpc.2015.03.003 [arXiv:1407.6129 [hep-ph]].
- [53] D. Abercrombie et al. *Dark Matter Benchmark Models for Early LHC Run-2 Searches: Report of the ATLAS/CMS Dark Matter Forum*, arXiv:1507.00966.
- [54] M. Baak et al. *HistFitter software framework for statistical data analysis*, *Eur.Phys.J.C* (2015), arXiv:1410.1280.
- [55] J. Abdallah et al. *Simplified Models for Dark Matter Searches at the LHC*, *Phys. Dark Uni.* 9-10 (2015) 8-23, arXiv:1506.03116.
- [56] J. Abdallah et al. *Simplified Models for Dark Matter and Missing Energy Searches at the LHC*, (2014), arXiv:1409.2893.
- [57] T. Jacques and K. Nordstrom, *Mapping monojet constraints onto Simplified Dark Matter Models*, *JHEP* 06 (2015) 142, arXiv:1502.05721.
- [58] T. Sjstrand et al. *An Introduction to PYTHIA 8.2*, *Comput. Phys. Comm.* 191 (2015) 159-177, arXiv:1410.3012.
- [59] R. M. Godbole, G. Mendiratta and T. M. P. Tait, *A Simplified Model for Dark Matter Interacting Primarily with Gluons*, *JHEP* 08 (2015) 064, arXiv:1506.01408.
- [60] ATLAS Collaboration, *Search for dark matter produced in association with a hadronically decaying vector boson in pp collisions at $\sqrt{s} = 13$ TeV with the ATLAS detector at the LHC*, ATLAS-CONF-2015-080 (2015).
- [61] M. L. Mangano et al. *Matching matrix elements and shower evolution for top-quark production in hadronic collisions*, *JHEP* 01 (2007), hep-ph/0611129.
- [62] ATLAS Collaboration, *Performance of jet substructure techniques for large-R jets in proton-proton collisions at $\sqrt{s} = 7$ TeV using the ATLAS detector*, *JHEP* 09 (2013) 076, arXiv:1306.4945.
- [63] M. Cacciari, G. P. Salam and G. Soyez, *FastJet user manual*, arXiv:1111.6097.
- [64] N. F. Bell et al, *Dark matter at the LHC: EFTs and gauge invariance*, *Phys. Rev. D* 92 (2015) 053008, arXiv:1503.07874.